JOURNAL OF SYNCHROTRON RADIATION
ISSN 1600-5775

A modified equally sloped algorithm based on the total variation algorithm in computed tomography for insufficient data

Lei Wang, Yong Guan,* Zhiting Liang, Liang Guo, Chenxi Wei, Ronghui Luo, Gang Liu and Yangchao Tian

National Synchrotron Radiation Laboratory, University of Science and Technology of China, 3#222, 42 Hezuohua South Road, Hefei, Anhui 230026, People's Republic of China.
*Correspondence e-mail: yongg@ustc.edu.cn

Received 22 October 2016
Accepted 19 January 2017

Edited by S. M. Heald, Argonne National Laboratory, USA

Keywords: computed tomography; total variation minimization; equally sloped tomography; limited-angle; few-view; noisy data.

Supporting information: this article has supporting information at journals.iucr.org/s

Computed tomography (CT) has become an important technique for analyzing the inner structures of material, biological and energy fields. However, there are often challenges in the practical application of CT due to insufficient data. For example, the maximum rotation angle of the sample stage is limited by sample space or image reconstruction from the limited number of views required to reduce the X-ray dose delivered to the sample. Therefore, it is difficult to acquire CT images with complete data. In this work, an iterative reconstruction algorithm based on the minimization of the image total variation (TV) has been utilized to develop equally sloped tomography (EST), and the reconstruction was carried out from limited-angle, few-view and noisy data. A synchrotron CT experiment on hydroxyapatite was also carried out to demonstrate the ability of the TV-EST algorithm. The results indicated that the new TV-EST algorithm was capable of achieving high-quality reconstructions from projections with insufficient data.

1. Introduction

Computed tomography (CT) has been widely used for obtaining three-dimensional (3D) images of objects without contact and invasion in many fields, such as material science (Midgley *et al.*, 2007), magnetic materials (Denbeaux *et al.*, 2001), environmental science (Patty *et al.*, 2009), energy science (Yang *et al.*, 2014) and biological science (Uchida *et al.*, 2009; Andrews *et al.*, 2011). Although CT has achieved many positive results, there are still some problems that influence its application. One major problem is the 'limited angle', that may be due to the following reasons: firstly, the maximum rotation angle of the sample stage, which is limited for the imaging of biological samples, because the sample holder impedes the X-rays when the angle is greater than 75° or less than −75° (Liang *et al.*, 2013); secondly, the sample has a plate-like geometry, such as a silicon chip, and, when it rotates to a high angle, X-rays cannot penetrate it; finally, there may be support structures as in a load-cell frame that obstruct the views at some angles (Duke *et al.*, 2014). Another problem is 'few view', where lower X-ray doses are delivered to the sample and less time is required for the experiment, especially for biological samples, which is a significant consideration. Noise is also always an unavoidable problem in the CT process and high noise tolerance becomes an important evaluation of the standard CT application (Milne & Subramaniam, 2009).

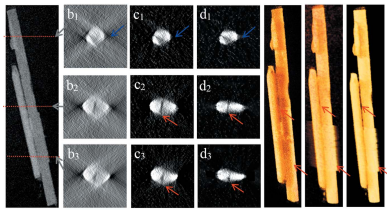

There are currently two popular types of algorithms for image reconstruction: the Fourier methods, which include filtered back-projection (FBP) (Mueller *et al.*, 1999), and the algebraic iterative reconstruction methods, which include the algebraic reconstruction technique (ART) and the simultaneous algebraic reconstruction technique (SART) (Liang *et al.*, 2016). Fourier methods have been the preferred choice by many CT manufacturers due to their lighter computational burden (Gengsheng, 2010). However, algebraic reconstruction methods, which formulate the reconstruction problem as a linear system of equations, can yield better results compared with Fourier methods, especially for few-view and limited-angle data.

Regardless of the method used, the set of projections is in polar coordinates, and the object is in Cartesian coordinates. Interpolation must be used in the reconstruction process, which introduces artificial errors in the finally reconstructed 3D object. Therefore, in 2005, Miao *et al.* first developed equally sloped tomography (EST) to avoid direct interpolations (Miao *et al.*, 2005). Recently, research has shown that EST could be used for 3D structure determination of nanomaterial at atomic-scale resolution and low-dose phase-contrast X-ray imaging of human breast cancers (Zhao *et al.*, 2012). Previous experimental results have proven that the EST algorithm showed an outstanding performance in dealing with few-view data, and only a few angles were needed to obtain a satisfactory result, thus reducing experimental time and the radiation dose to the sample. However, when dealing with limited-angle or noisy data, EST still had some problems. Some simulation experiments showed that EST may introduce additional noise and artifacts, especially in areas where the image changes drastically. This phenomenon also has been found in the current study and is described in §3.2 and §3.3. Thus, previous works on EST have mainly focused on maintaining the quality of reconstructed images while reducing the number of projections and eliminating the influence of noise (Fahimian *et al.*, 2010).

Several years ago, an iterative reconstruction algorithm based on the minimization of the image total variation (TV) was used to improve image reconstruction quality (Velikina *et al.*, 2007). The TV of an image is a numerical quantity that reflects the intensity change of local regions of an image. In that work, the authors indicated that the TV algorithm could handle the various insufficient data problems in fan-beam CT. At the same time, the TV algorithm could be generalized to cone-beam CT as well as other tomographic imaging modalities (Sidky *et al.*, 2006).

In this work, a modified EST algorithm based on the TV algorithm was proposed and applied in CT reconstructions with few-view, limited-angle and noisy data. The Shepp–Logan phantom was used as an example in simulation experiments to inspect the algorithm in different situations, and the results of the TV-EST algorithm were shown and compared with those of the traditional FBP and original EST algorithm. Finally, a synchrotron CT experiment on hydroxyapatite was carried out to demonstrate the ability of this algorithm.

2. TV-based EST reconstruction algorithm

2.1. Imaging model

The general theory for the CT system discussed here involves a linear transformation

$$WX = Y \tag{1}$$

where the system matrix $W = [w_{i,j}]_{N\times M}$ composed of N row vectors $\overrightarrow{W_i}$ that yield each projection data point, and $\overrightarrow{Y_{i,j}} = \overrightarrow{W_i} \times \overrightarrow{X_j}$, and where X is the unknown image and Y is the measured projection data. We seek to obtain an image represented by the vector X from the data vector Y and the system matrix W. However, the data from vector Y always contain insufficient data, so it is difficult to calculate the values of the image vector X by inverting equation (1) directly.

2.2. EST reconstruction

A new form of the fast Fourier transform (FFT), known as the pseudo-polar fast Fourier transform (PPFFT), was applied in the EST iterative algorithm (Lee *et al.*, 2008). Fig. 1 shows the PPFFT grid points in the Fourier domain located on the equally sloped lines but not equally angled lines. PPFFT has been proven to be mathematically exact, geometrically faithful and invertible (Averbuch *et al.*, 2008).

2.3. TV reconstruction

To solve the linear system represented in equation (1), the TV minimization was considered an effective method of obtaining high-quality reconstructed images from insufficient data that implemented the following optimization program. Find X when

$$\min \|X_{\rm TV}\| \qquad \text{such that} \qquad WX = Y. \tag{2}$$

Sidky *et al.* (2006) have developed a TV algorithm (POCS-TV) and described it in detail in their paper solving equation (2). In that algorithm, the minimization of the image TV was performed by the gradient descent method (Candès *et al.*, 2006), and the constraints imposed by the known projection data were incorporated by projection on convex sets (POCS)

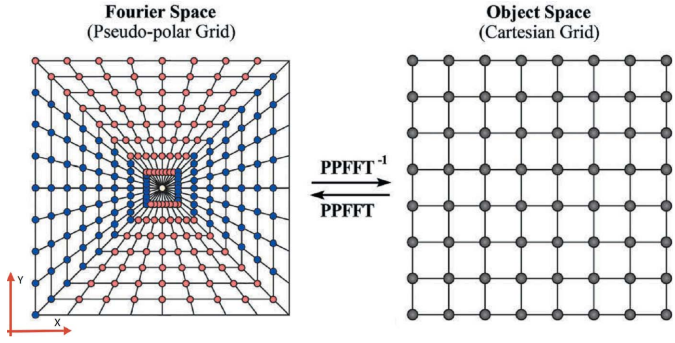

Figure 1
Pseudo-polar grid and pseudo-polar fast Fourier transform (PPFFT). For an $N \times N$ Cartesian grid where $N = 8$ in this case, the corresponding pseudo-polar grid is defined by a set of $2N$ lines, with each line consisting of $2N$ grid points mapped out on N concentric squares.

[§15.4.5 of Barrett & Myers (2013)]. They used the following approximate derivative and referred to the resulting gradient vector as $\vec{G}_{i,j}$,

$$\begin{aligned} G_{i,j} &= \frac{\partial \|X\|_{\mathrm{TV}}}{\partial X_{i,j}} \\ &\simeq \frac{(X_{i,j}-X_{i-1,j})+(X_{i,j}-X_{i,j-1})}{\left[\varepsilon+(X_{i,j}-X_{i-1,j})^2+(X_{i,j}-X_{i,j-1})^2\right]^{1/2}} \\ &\quad -\frac{(X_{i+1,j}-X_{i,j})}{\left[\varepsilon+(X_{i+1,j}-X_{i,j})^2+(X_{i+1,j}-X_{i+1,j-1})^2\right]^{1/2}} \\ &\quad -\frac{(X_{i+1,j}-X_{i,j})}{\left[\varepsilon+(X_{i,j+1}-X_{i,j})^2+(X_{i,j+1}-X_{i-1,j+1})^2\right]^{1/2}}. \end{aligned} \tag{3}$$

ε is a small positive number, $\varepsilon = 10^{-8}$. The number n is defined as the iteration number that labels the iterative process, and the TV gradient descent could be defined as

(A) Positivity constraint:

$$X_{i,j}(n-1) = \begin{cases} X_{i,j}(n-1)_{\mathrm{orig}} & X_{i,j}(n-1) \geq 0, \\ 0 & X_{i,j}(n-1) < 0. \end{cases} \tag{4}$$

(B) Gradient descent initialization:

$$d_A = \left\| X(n-1)_{\mathrm{orig}} - X(n-1) \right\|_2. \tag{5}$$

(C) Gradient descent:

$$\vec{G}_{i,j}(n-1) = \left. \frac{\partial \|\vec{X}\|}{\partial X_{i,j}} \right|_{X_{i,j}=X_{i,j}(n-1)}, \tag{6}$$

$$G(n-1) = \frac{\vec{G}(n-1)}{\left|\vec{G}(n-1)\right|}, \tag{7}$$

$$X(n) = X(n-1) - a d_A G(n-1), \tag{8}$$

where X is the image matrix and $X(n)$ represents the matrix that is obtained after n cycles. The distance d_A provides a measure for the difference between the image estimated before the TV gradient descent and the image estimated after the enforcement of positivity. The gradient descent procedure is controlled by specifying the parameter a. In this paper, a = 0.2 was selected.

2.4. TV-EST algorithm

As mentioned above, EST still had some problems when dealing with insufficient data. Therefore, in this study, a new modified algorithm (TV-EST) was proposed, which was based on the TV algorithm introduced in §2.2 and §2.3. The steps of the modified algorithm have two important components: the EST-step, which is counted by n and enforces consistency of the results and projection data, and the TV-step, which is counted by m and reduces the TV of the image. Fig. 2 shows an overview of our TV-EST algorithm.

Importation: projections Y and the angle θ of projections

Initialization: total number of iterations t, each step count numbers n and m, the parameter a

Algorithm:

$X_{est}(0) = 0$; $t = 0$

while (step criterion is not met) do

Begin

$t = t + 1$

For $n = 1{:}N_{max}$

$X_{est}(n) = EST[X_{est}(n-1)]$

End

$X_{tv}(0) = X_{est}(N_{max})$

For $m = 1{:}M_{max}$

$X_{tv}(m) = TV[X_{tv}(m-1)]$

End

$X_{est}(0) = X_{tv}(M_{max})$

End

Output: X

Figure 2
Basic steps of the TV-EST algorithm.

3. Simulation results

Here, a series of simulation experiments are described to evaluate the performance of the TV-EST algorithm when it meets with insufficient data. Moreover, the results of the FBP and original EST algorithm are compared with that of the TV-EST algorithm. The true image was taken to represent the Shepp–Logan phantom shown in Fig. 3(a) presented on a 512 × 512 pixel grid, and the central line profile of the phantom is presented in Fig. 3(b). This phantom was often used for evaluating tomographic reconstruction algorithms. In

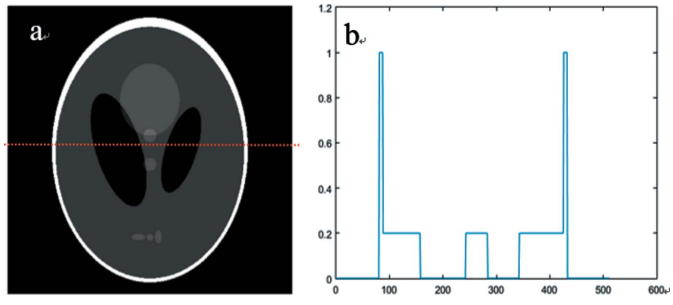

Figure 3
(a) The true Shepp–Logan phantom. (b) The central line profile of the phantom.

this study, δ was defined as the evaluation factor to quantitative statistics comparing the results of each case with the true Shepp–Logan values. These were calculated as follows,

$$\delta = \left[\sum \left(X_{i,j} - X_{\rm orig}\right)^2 / N\right]^{1/2}, \qquad (9)$$

where $X_{i,j}$ and $X_{\rm orig}$ are the values of the pixels in the reconstructed image and the true Shepp–Logan image, respectively, and N is the total number of pixels. A smaller δ represents a higher reconstruction quality.

3.1. Few-view results

Images from 25-, 20- and 15-view projection data were reconstructed by using the FBP, EST and TV-EST algorithms, respectively, as shown in Fig. 4. With a decrease of the number of the projections, artifacts become more serious in the reconstructed image for the three reconstructed algorithms. However, among reconstructed results from 15-view projections using the FBP, EST and TV-EST algorithms, the FBP algorithm is the worst, indicating that it has no ability to deal with this few-view case. Meanwhile, it is easy to visually distinguish the different compositions and their profiles in Fig. 4(*i*). The reconstructed results of the TV-EST are shown to be better than those of the FBP and EST algorithms. When projections increase to 25 views, reconstructed results of the TV-EST [Fig. 4(*g*)] are closest to those of the original image. For a quantitative comparison, we also demonstrate the central line profile of the images reconstructed by 25-view projections in the last row of Fig. 4 and the values of the evaluation factor in Table 1. The central line profile of the images also shows that Fig. 4(*l*) is a closer match to the original phantom than Figs. 4(*j*) and Fig. 4(*k*), and there is very little fluctuation in Fig. 4(*l*). As shown in Table 1, the values of TV-EST are the smallest of all the algorithms, indicating that it has the best reconstruction results.

3.2. Limited-angle results

The limited-angle data were also a challenge in the CT process due to limited sample space or overmuch thickness of the sample (Yao *et al.*, 2016). For example, for X-ray nano-CT, the angle range was usually limited to -75° to 75° due to the use of a flat sample holder. According to this situation, reconstructed results of the Shepp–Logan phantom based on the projections with -85° to 85°, -75° to 75° and -65° to 65° ranges using the three reconstructed methods are presented. Fig. 5 shows the images reconstructed from the limited-angle data mentioned above by the FBP, EST and TV-EST algorithms, and central line profiles of the images, and Table 2 gives the values of the evaluation factors. FBP suffers more artifacts than the other two algorithms. However, the TV-EST and EST algorithms can overcome the influence of limited-angle to provide relatively accurate reconstructed results. Furthermore, the central line profiles of the images reconstructed from the projection with an angle range of -75° to 75° are presented in Figs. 5(*j*)–5(*l*), and the evaluation

Table 1
Evaluation factor δ for the results in Fig. 4.

	25-view	20-view	15-view
FBP	0.195	0.227	0.276
EST	0.031	0.066	0.095
TV-EST	0.009	0.034	0.056

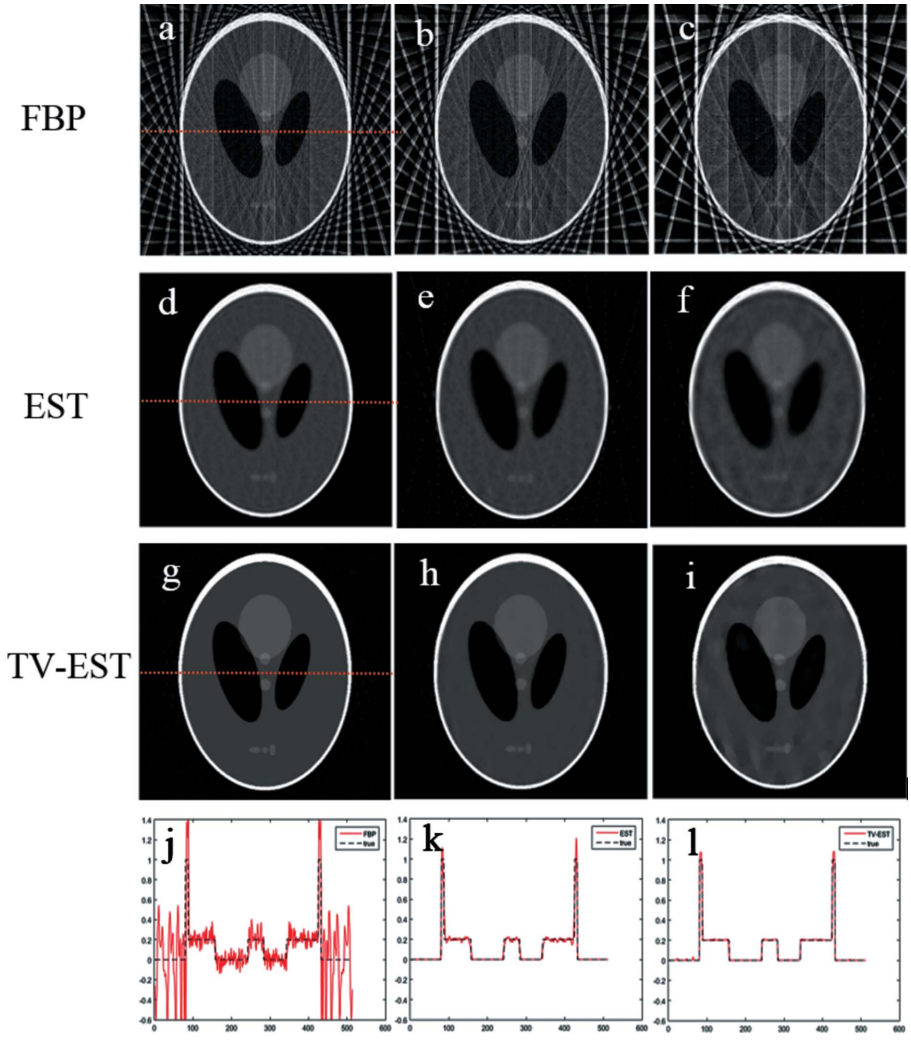

Figure 4
Images reconstructed by (*a*–*c*) the FBP, (*d*–*f*) EST and (*g*–*i*) TV-EST algorithms from few-view projections. (*a*, *d*, *g*) 25-view projections, (*b*, *e*, *h*) 20 projections and (*c*, *f*, *i*) 15 projections. (*j*, *k*, *l*) Central line profiles of (*a*, *d*, *g*).

Table 2
Evaluation factor δ for the results in Fig. 5.

	−85° to 85°	−75° to 75°	−65° to 65°
FBP	0.030	0.058	0.119
EST	0.025	0.038	0.053
TV-EST	0.013	0.019	0.032

factor values are shown in Table 2. When comparing the FBP, EST and TV-EST methods, the reconstructed accuracy of the FBP method is found to be worst since its central line profiles fluctuate most strongly, and its δ is the largest, which further indicates that FBP is not a suitable tool for reconstructing limited-angle projections. Additionally, the EST algorithm provides relatively accurate reconstructed results, although it also introduces some extra noise as shown in Fig. 5(*k*). The TV-EST algorithm does not have this drawback [Fig. 5(*l*)].

3.3. Noisy data results

Noise has always been an unavoidable problem in the actual CT process. To inspect the degree of noise resistance of the TV-EST algorithm, Gaussian noise was introduced in the projection data in this study and 50 dB, 45 dB and 40 dB SNR (signal-to-noise ratio) were selected. Figs. 6(*a*)–6(*i*) show the reconstructed images from the projections with these three SNRs using three reconstructed algorithms. Based solely on the images, it is difficult to compare the differences of the various algorithms, thus the central line profiles of all reconstructed images were given as shown in Figs. 6(*j*)–6(*r*). Table 3 shows the evaluation factor values for the different algorithms. The anti-noise ability of the EST algorithm can be clearly seen as the weakest among the three algorithms, while the TV-EST algorithm shows the best performance to deal with different SNRs. This also indicated that strong anti-noise ability is one of the important advantages of the advanced TV method.

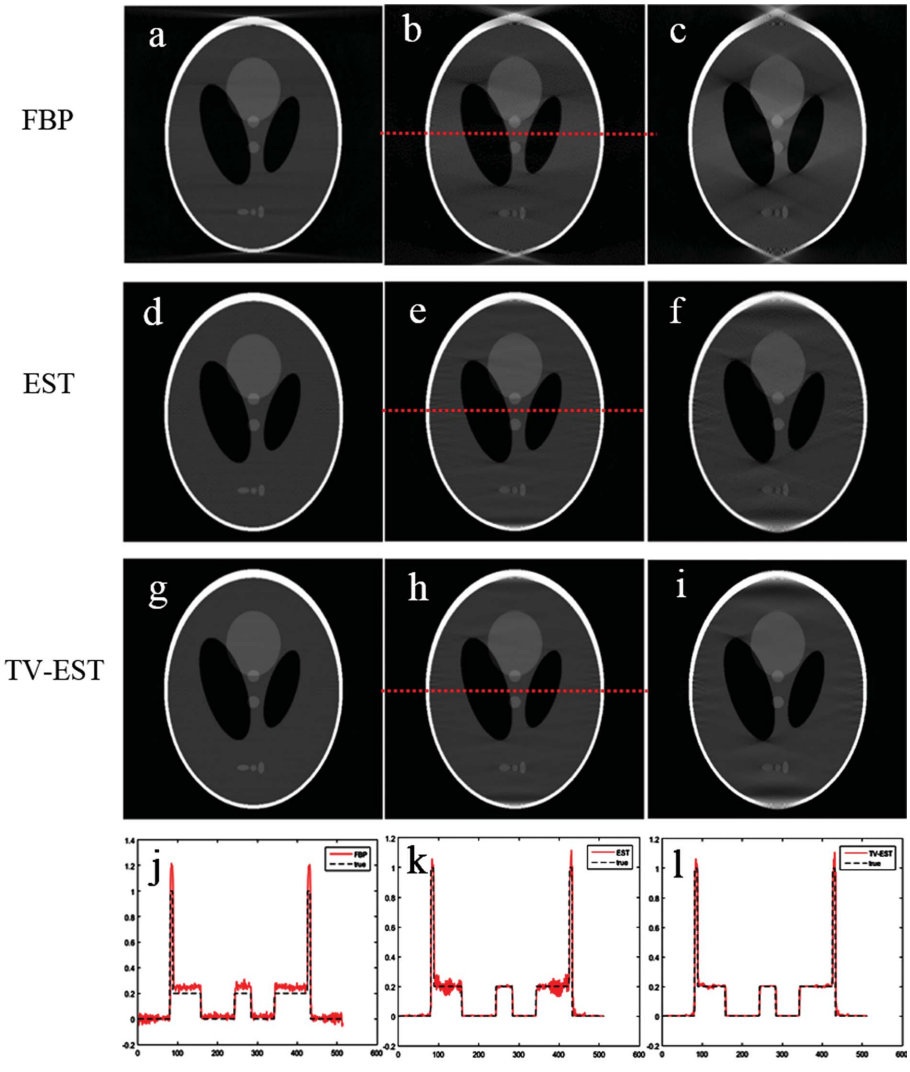

Figure 5
Images reconstructed from the projections with angle ranges of −85° to 85°, −75° to 75° and −65° to 65° using the FBP (*a*–*c*), EST (*d*–*f*) and TV-EST (*g*–*i*) algorithms. (*j*, *k*, *l*) Central line profiles of (*b*, *e*, *h*), respectively.

3.4. Complicated situation

Experiments considering all factors mentioned above were carried out to test the performance of the three algorithms synthetically. As shown in Fig. 7, the images were reconstructed under the following conditions: 25-view projections, −75° to 75°, 50 dB SNR. Even under such extreme conditions the TV-EST algorithm can yield a positive result. Furthermore, the central line profile matches with that of the original phantom in Fig. 7(*f*), and the value of δ is also satisfactory in Table 4. This proves that the TV-EST algorithm developed in this study can deal with complex cases under extreme conditions and yield satisfactory results.

3.5. Algorithm performance

Here, the computational performance of the algorithms is addressed. The computation times for each of the reconstructions in Figs. 4–7 are shown in Table 5. In this study, a computer equipped with four Intel processors clocked at 3.20 GHz (using a single core) and 8 GB RAM was used to compute the data. Since the EST algorithm is an iterative algorithm, whereas the FBP algorithm is an analytic algorithm, when using them to deal with the same problem the computation time of these two methods will differ greatly. The traditional FBP algorithm requires only a few seconds. However, EST and TV-EST require a few minutes to generate results. Additionally, in Fig. 4,

Table 3
Evaluation factor δ for the results in Fig. 6.

	50 dB	45 dB	40 dB
FBP	0.034	0.040	0.076
EST	0.041	0.051	0.095
TV-EST	0.018	0.021	0.035

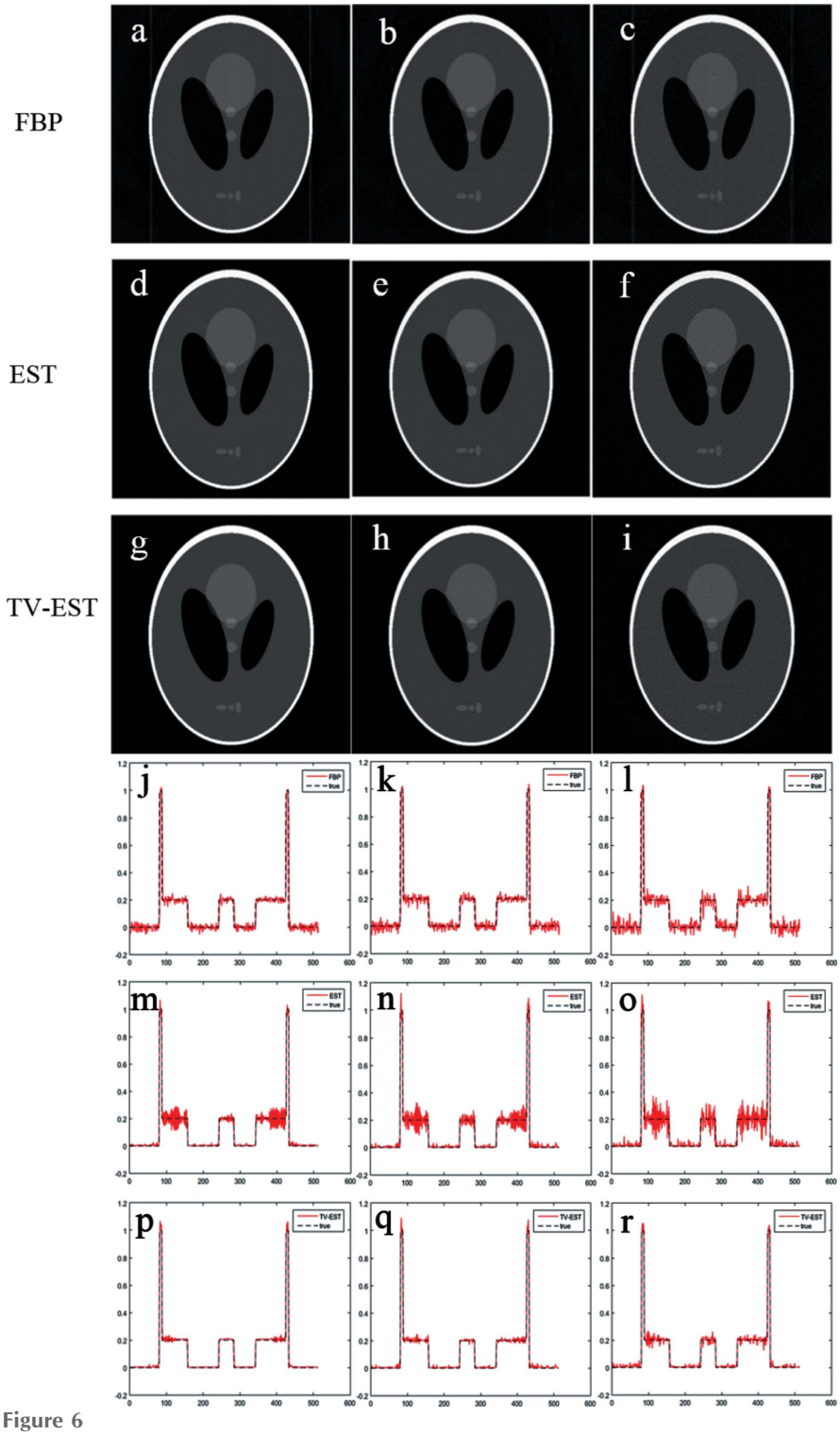

Figure 6
Images reconstructed from the projections with 50 dB, 45 dB and 40 dB SNR using the FBP [Figs. 5(*a*)–5(*c*)], EST [Figs. 5(*d*)–5(*f*)] and TV-EST [Figs. 5(*g*)–5(*i*)] algorithms. (*j*–*r*) Central line profiles of (*a*–*i*), respectively.

because of the few-view projections, larger iteration numbers were adopted to achieve a satisfactory result, which shows that the process took a very long time. During this time we found that the TV-EST algorithm converged faster and required a smaller number of iterations than the EST algorithm. Therefore its computation time was shorter than that of EST. Although the iterative algorithm has a long computation time, with the development of science and technology we believe that advances in computing devices and methods, such as parallel computing, can shorten the computation time of TV-EST. This is studied in our next step.

4. 3D reconstruction of hydroxyapatite

Here, in order to further test the performance of our algorithm, synchrotron CT experiments were carried out by soft X-ray microscope at beamline BL07W at the National Synchrotron Radiation Laboratory in Hefei, China. This imaging system can provide transmission of full-field imaging of samples from 250 eV to 1800 eV with a 30 nm spatial resolution. First, an X-ray is focused onto the sample by an elliptical capillary condenser, and then a magnified image is formed by an objective zone plate lens onto a 16-bit 1024 × 1024 CCD detector. In this study, the hydroxyapatite, which is a kind of calcium phosphate, was used as the sample to be imaged. At first the hydroxyapatite was dissolved in alcohol, and then the solution was dropped onto a copper grid. Due to the limitation of the copper grid, only a portion of the projections were obtained because the sample holder impedes the X-rays when the angle is greater than 65° or less than −65°. Fig. 8 shows the 3D reconstruction results of the FBP, EST and TV-EST methods. These results indicate that the sample exhibits a flat columnar structure. By comparison, several instances of artifacts and background noise, which interfered with our observation, are labelled by the blue arrows in Fig. 8(*b*). However, the EST and TV-EST algorithms both suppress background noise effectively, and the samples are highlighted from the background. Two different column sections were clearly distinguished through the slice images in Figs. 8(*c*) and 8(*d*). Carefully comparing the areas marked by red arrows shows the effect of our algorithm, especially the

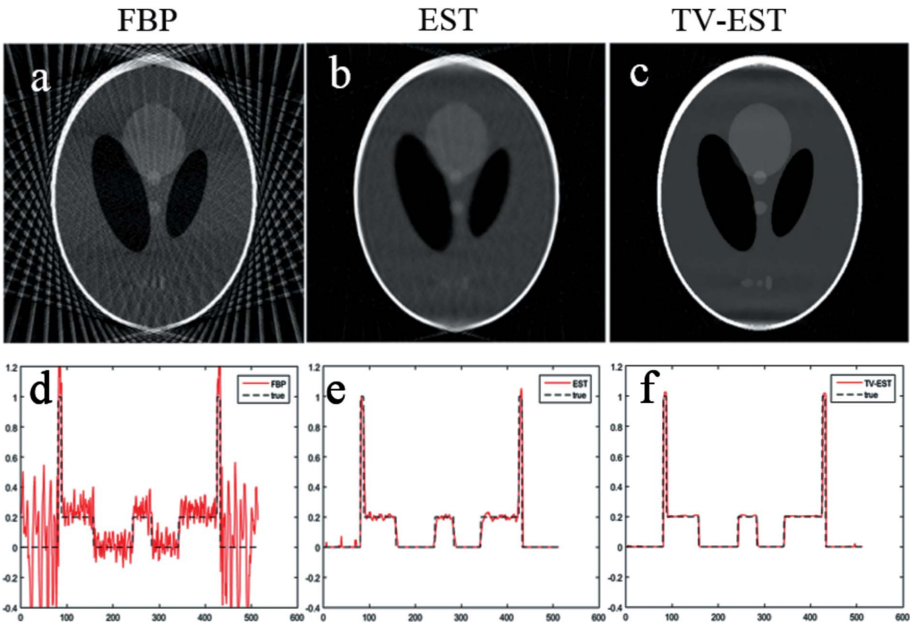

Figure 7
Images reconstructed by the FBP (*a*), EST (*b*) and TV-EST (*c*) algorithms on the condition of 25-view projections, −75° to 75° and 50 dB. (*d*, *e*, *f*) Central line profiles of (*a*, *b*, *c*), respectively.

compensation for the loss of the angle. The reconstructed image quality is better, clearer and the boundary of the object is easier to divide in Fig. 8(*d*) than in Fig. 8(*c*). In order to compare the reconstruction results quantitatively, the diameters of reconstructed hydroxyapatite in Figs. 8(*e*)–8(*g*) were calculated and compared with those of the two-dimensional projections in Fig. 8(*a*). Table 6 shows the result. Due to the influence of artifacts, the diameters were overestimated when the FBP or EST results were used for segmentation. However, the difference between the diameters of two-dimensional projections and the value calculated by TV-EST is the smallest, which indicates that the results of TV-EST are more accurate.

Table 4
Evaluation factor δ for the results in Fig. 7.

FBP	EST	TV-EST
0.198	0.039	0.019

5. Discussion and conclusion

In this paper, a TV-EST algorithm was developed for accurate image reconstruction in CT processes under various imperfect conditions, including few-view, limited-angle and noisy data problems. This algorithm was tested using simulation data and CT experiments and compared with FBP and EST algorithms. The results indicate that the TV-based EST is a powerful algorithm that provides more accurate reconstructions under these extreme conditions and exhibits some advantages that other algorithms do not have due to the excellent capabilities of PPFFT and inverse PPFFT applied in EST. Additionally, the advanced TV method also

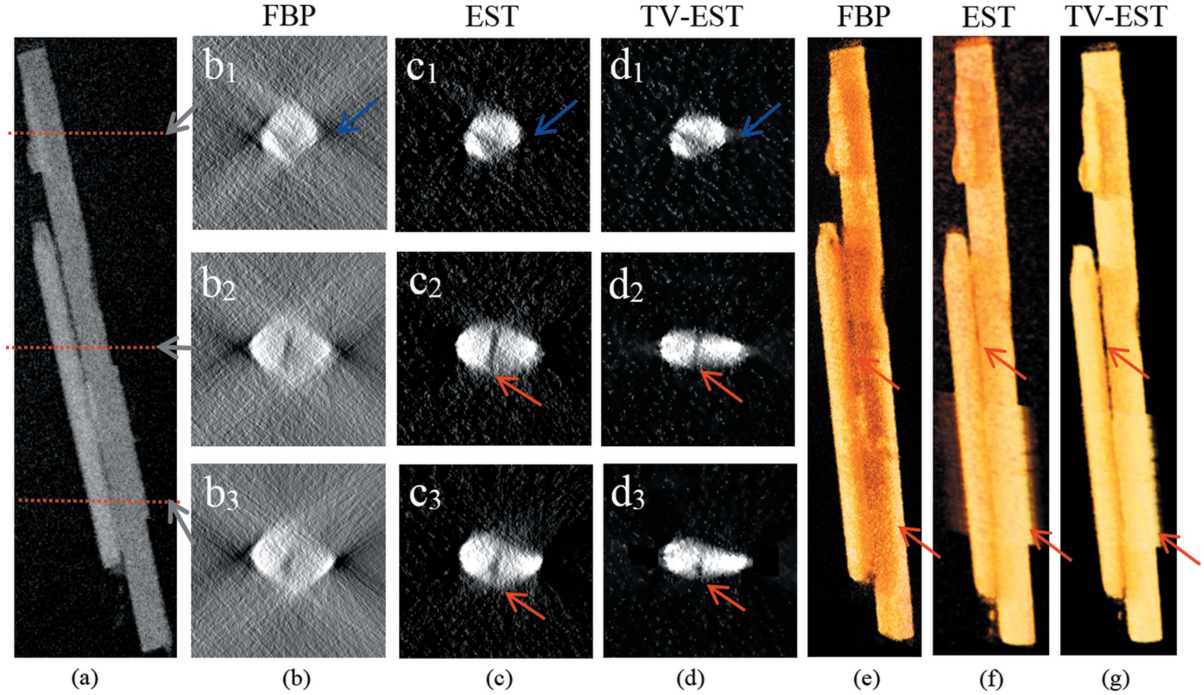

Figure 8
Hydroxyapatite reconstructed from the projections with angle ranges of −65° to 65°. (*a*) Representative projection. The slices along the red imaginary lines in (*a*) are shown in (*b*), (*c*) and (*d*), which were reconstructed from the FBP, EST and TV-EST algorithms, respectively. (*e*, *f*, *g*) 3D images of the hydroxyapatite reconstructed by the FBP, EST and TV-EST algorithms, respectively.

Table 5
Computation time t (s) for each of the reconstructions in Figs. 4–7.

	(*a*)	(*b*)	(*c*)	(*d*)	(*e*)	(*f*)	(*g*)	(*h*)	(*i*)
Fig. 4	0.1	0.1	0.1	613	620	631	401	424	431
Fig. 5	2.2	1.9	1.7	51	49	50	39	42	41
Fig. 6	2.3	2.3	2.3	34	38	37	24	26	25
Fig. 7	0.1	648	456						

Table 6
Diameters (μm) of the sample in Fig. 8.

		Left	Right	Left	Right
Projection	1.706	1.005	1.097	1.066	1.158
FBP	1.889 (b1)	1.219 (b2)	1.371 (b2)	1.432 (b3)	1.493 (b3)
EST	1.798 (c1)	1.066 (c2)	1.188 (c2)	1.158 (c3)	1.310 (c3)
TV-EST	1.737 (d1)	1.005 (d2)	1.067 (d2)	1.066 (d3)	1.188 (d3)

effectively compensates for the insufficient data. With the wide application of CT in medical, industrial or other aspects, a variety of different challenges will be met. Therefore, a TV-based EST algorithm will have much practical significance. We are currently investigating the application of the TV-based EST algorithm to fast 3D CT, and there are a number of imperfect sampling situations that have practical significance (Liu *et al.*, 2016). For example, to reduce the radiation exposure to the patient and speed up computations, more sparse projection angles are intentionally adopted. Moreover, due to the intensity of the dose, when the patient is lying on their side, X-rays may be impenetrable, which introduces the limited-angle problem. At the same time, we will continue to improve our algorithm and optimize its performance.

Acknowledgements

This work was supported by grants from the Major State Basic Research Development Program of China (973 Program) (No. 2012CB825804), the National Science Foundation of China (Nos. 11275204, 11475175 and 11405175), and the National Key Research and Development Program of China (2016YFA0400902).

References

Andrews, J. C., Meirer, F., Liu, Y., Mester, Z. & Pianetta, P. (2011). *Microsc. Res. Tech.* **74**, 671–681.
Averbuch, A., Coifman, R. R., Donoho, D. L., Israeli, M. & Shkolnisky, Y. (2008). *SIAM J. Sci. Comput.* **30**, 764–784.
Barrett, H. H. & Myers, K. J. (2013). *Foundations of Image Science.* New York: John Wiley and Sons.
Candès, E. J., Romberg, J. & Tao, T. (2006). *IEEE Trans. Inf. Theory*, **52**, 489–509.
Denbeaux, G., Anderson, E., Chao, W., Eimüller, T., Johnson, L., Köhler, M., Larabell, C., Legros, M., Fischer, P., Pearson, A., Schütz, G., Yager, D. & Attwood, D. (2001). *Nucl. Instrum. Methods Phys. Res. A*, **467–468**, 841–844.
Duke, E. M., Razi, M., Weston, A., Guttmann, P., Werner, S., Henzler, K., Schneider, G., Tooze, S. A. & Collinson, L. M. (2014). *Ultramicroscopy*, **143**, 77–87.
Fahimian, B. P., Mao, Y., Cloetens, P. & Miao, J. (2010). *Phys. Med. Biol.* **55**, 5383–5400.
Gengsheng, L. Z. (2010). *Medical Image Reconstruction: A Conceptual Tutorial.* Beijing: Higher Education Press.
Lee, E., Fahimian, B. P., Iancu, C. V., Suloway, C., Murphy, G. E., Wright, E. R., Castaño-Díez, D., Jensen, G. J. & Miao, J. (2008). *J. Struct. Biol.* **164**, 221–227.
Liang, Z., Guan, Y., Liu, G., Bian, R., Zhang, X., Xiong, Y. & Tian, Y. (2013). *Proc. SPIE*, **8851**, 885117.
Liang, Z., Guan, Y., Liu, G., Chen, X., Li, F., Guo, P. & Tian, Y. (2016). *J. Synchrotron Rad.* **23**, 606–616.
Liu, Y., Kiss, A. M., Larsson, D. H., Yang, F. & Pianetta, P. (2016). *At. Spectrosc.* **117**, 29–41.
Miao, J., Förster, F. & Levi, O. (2005). *Phys. Rev. B*, **72**, 052103.
Midgley, P. A., Ward, E. P., Hungría, A. B. & Thomas, J. M. (2007). *Chem. Soc. Rev.* **36**, 1477–1494.
Milne, J. L. & Subramaniam, S. (2009). *Nat. Rev. Microbiol.* **7**, 666–675.
Mueller, K., Yagel, R. & Wheller, J. J. (1999). *IEEE Trans. Med. Imaging*, **18**, 519–537.
Patty, C., Barnett, B., Mooney, B., Kahn, A., Levy, S., Liu, Y., Pianetta, P. & Andrews, J. C. (2009). *Environ. Sci. Technol.* **43**, 7397–7402.
Sidky, E. Y., Kao, C.-M. & Pan, X. (2006). *J. X-ray Sci. Technol.* **14**, 119–139.
Uchida, M., McDermott, G., Wetzler, M., Le Gros, M. A., Myllys, M., Knoechel, C., Barron, A. E. & Larabell, C. A. (2009). *Proc. Natl Acad. Sci.* **106**, 19375–19380.
Velikina, J., Leng, S. & Chen, G.-H. (2007). *Proc. SPIE*, **6510**, 651020.
Yang, F., Liu, Y., Martha, S. K., Wu, Z., Andrews, J. C., Ice, G. E., Pianetta, P. & Nanda, J. (2014). *Nano Lett.* **14**, 4334–4341.
Yao, S., Fan, J., Zong, Y., He, Y., Zhou, G., Sun, Z., Zhang, J., Huang, Q., Xiao, T. & Jiang, H. (2016). *Appl. Phys. Lett.* **108**, 123702.
Zhao, Y., Brun, E., Coan, P., Huang, Z., Sztrókay, A., Diemoz, P. C., Liebhardt, S., Mittone, A., Gasilov, S., Miao, J. & Bravin, A. (2012). *Proc. Natl Acad. Sci.* **109**, 18290–18294.